Catalysis Today 145 (2009) 279–287

Contents lists available at ScienceDirect

Catalysis Today

journal homepage: www.elsevier.com/locate/cattod

Dynamic in situ observation of automotive catalysts for emission control using X-ray absorption fine structure

Yasutaka Nagai [a,*], Kazuhiko Dohmae [a], Kentaro Teramura [b], Tsunehiro Tanaka [b], Gemma Guilera [c,1], Kazuo Kato [d], Masaharu Nomura [e], Hirofumi Shinjoh [a], Shin'ichi Matsumoto [f]

[a] TOYOTA Central R&D Labs., Inc., Nagakute, Aichi 480-1192, Japan
[b] Department of Molecular Engineering, Kyoto University, Kyoto 615-8510, Japan
[c] European Synchrotron Radiation Facility, Grenoble F-38043, France
[d] SPring-8, Japan Synchrotron Radiation Research Institute, Sayo, Hyogo 679-5198, Japan
[e] Photon Factory, Institute of Materials Structure Science, High Energy Accelerator Research Organization, Tsukuba, Ibaraki 305-0801, Japan
[f] TOYOTA Motor Corporation, Toyota, Aichi 471-8572, Japan

ARTICLE INFO

Article history:
Available online 11 December 2008

Keywords:
Ceria–zirconia
Oxygen storage capacity
Platinum
Sintering
XAFS
Automotive catalyst

ABSTRACT

Two main pivotal subjects of research in automotive catalysts were studied by modern X-ray absorption analysis techniques. One is oxygen storage/release behaviour, and the other is sintering inhibition of Pt particles. First, three types of CeO_2–ZrO_2 (Ce:Zr = 1:1 molar ratio) compounds with different oxygen storage/release capacities and different structural properties were prepared, and the valence change of Ce as a function of temperature during oxygen release/storage processes was investigated. The reduction of surface Ce mainly occurred in the range 100–170 °C, and the reduction of bulk Ce progressed at high temperatures of 170 °C and above. The Ce reduction behaviour depended not only on the homogeneity of the Ce and Zr for bulk reduction at high temperatures but also on the particle size of the CeO_2–ZrO_2 samples for surface reduction at low temperatures. Secondly, sintering inhibition of Pt in Pt/Al_2O_3, Pt/MgO and Pt/ceria-based catalysts after 800 °C ageing in air was studied. We found that the Pt–O–M (M = Mg, Ce) bond acted as an anchor and inhibited the sintering of Pt particles on MgO or ceria-based oxide. Especially, it was noteworthy that the Pt–O–Ce^{4+} bond on the ceria-based support breaks easily through the reduction of Ce ($Ce^{4+} \rightarrow Ce^{3+}$) during the usual stoichiometric and reducing conditions.

1. Introduction

This study is concerning the automotive catalysts to remove the harmful emission from automotive engines. Today, the automobile society is growing on the global scale, and vehicles are essential to make our living more convenient and richer. On the other hand, vehicles have a great effect on the global environment and natural resources. Recently, due to increasing demands for global environmental protection, more stringent regulations have been imposed on the automobile industry. Automobile companies are striving to purify automobile exhaust emissions. Consequently, there is a strong demand to produce more advanced automotive catalysts by technical innovation. Here, we present the study of automotive catalysts using modern X-ray absorption fine structure (XAFS) techniques at SPring-8 (Hyogo, Japan), ESRF (Grenoble, France) and KEK PF (Tsukuba, Japan).

Basically, the automobile three-way catalysts (TWCs) consist of precious metals such as Pt and Rh, supports such as Al_2O_3, and ceria-based oxide as an oxygen storage component [1–3]. The precious metal acts as the active site to simultaneously purify harmful automotive exhaust such as nitrogen oxides (NO_x), carbon monoxide (CO) and unburned hydrocarbons (HC). Exhaust condition from a gasoline engine changes quickly and dramatically, in response to a driver's operation. Temperature goes up to around 1000 °C, and gas condition fluctuates rapidly between oxidative and reductive atmospheres. Therefore, in situ dynamic observation of TWC affords the key to the development of advanced catalysts.

There are two main important subjects of research in TWC with higher catalytic efficiency and longer longevity. One is the oxygen storage/release capacity (OSC) promoter, and the other is the sintering inhibition of precious metal particles as the active site for catalytic reaction. As for the OSC material, in the TWCs, CeO_2–ZrO_2 mixed oxide is widely used as a promoter due to its high OSC based

* Corresponding author. Fax: +81 561 63 6150.
E-mail address: e1062@mosk.tytlabs.co.jp (Y. Nagai).
[1] Current address: ALBA-CELLS, Bellaterra, Barcelona, Spain.

0920-5861/$ – see front matter © 2008 Elsevier B.V. All rights reserved.
doi:10.1016/j.cattod.2008.10.031

on the reversible redox Ce^{4+}/Ce^{3+} reaction ($CeO_2 \leftrightarrow CeO_{2-x} + x/2O_2$; $x = 0$–0.5). Ceria stores oxygen under oxygen excess conditions and releases it under oxygen deficient conditions in order to maintain the stoichiometric conditions. The highest catalytic performance is attained at stoichiometric conditions. Therefore, the electronic and structural dynamics of CeO_2–ZrO_2 during the oxygen storage/release processes in the working state is pivotal to understand the fundamental knowledge. Recently, several studies by in situ techniques have been conducted on the physical properties and structure of CeO_2–ZrO_2, and significant progress in knowledge has been made. Overbury et al. reported the reduction behaviour (oxygen release process) of CeO_2–ZrO_2 mixed oxides using in situ X-ray absorption near-edge structure (XANES) [4]. Fernández-García et al. investigated the physical and chemical properties of CeO_2–ZrO_2 nanoparticles using synchrotron-based techniques such as time-resolved X-ray diffraction (XRD) [34]. Moreover, Iwasawa and coworkers showed the extremely elegant and novel finding of the dynamic behaviour of a Pt/ordered CeO_2–ZrO_2 (referred to as "κ-$Ce_2Zr_2O_8$") during the oxygen storage/release processes, by using in situ time-resolved energy-dispersive XAFS (DXAFS) technique [5]. In this report, in order to deepen the understanding, we prepared three types of CeO_2–ZrO_2 (Ce:Zr = 1:1 molar ratio) compounds with different OSC and different structural properties, including the κ-$Ce_2Zr_2O_8$. The valence change of Ce as a function of temperature during the oxygen release/storage processes for these samples was studied.

Secondly, concerning the sintering inhibition of precious metal particles, Pt catalysts after high-temperature ageing in an oxidative atmosphere was investigated. The precious metal particles are a few nanometer (nm) in diameter and are dispersed on a support oxide. When the TWC is exposed to high-temperatures of about 800 °C and above, the precious metal will agglomerate and sinter, lowering the active surface area [6–9]. Generally, the sintering of the precious metal particles during operation is considered to cause a decrease in the catalytic activity, i.e. degradation. Specifically, the activity of Pt-supported catalysts significantly decreases after high-temperature ageing in an oxidative atmosphere due to the sintering of Pt particles when compared to in a reductive atmosphere [6,7]. Therefore, the development of highly durable catalysts without Pt sintering in an oxidative atmosphere is strongly required in automotive industrial research. Several research groups have reported that ceria-based oxide support stabilizes Pt metal dispersion through Pt–ceria complex under oxidizing condition [9–12]. In our previous study, we showed that the Pt–O–Ce bond acted as an anchor and inhibited the sintering of Pt particles on ceria-based oxide [13]. On the other hand, it is considered that Pt^0 (metal) is the active site for the catalytic reaction in automotive exhaust condition. The ceria-based support could stabilize a high valence state (Pt^{2+} or Pt^{4+}) of Pt after an oxidative ageing. Pt on ceria-based support has to be reducible during the catalytic reaction. Therefore, in this report, we conducted the systematic investigation on both the Pt sintering inhibition and Pt reduction for catalytic reaction in Pt/Al_2O_3, Pt/MgO, Pt/ceria-based oxide catalysts using various types of XAFS techniques.

2. Experimental

2.1. Study of redox behaviour of ceria–zirconia mixed oxides

2.1.1. Preparation

The following three methods were utilized to prepare three types of CeO_2–ZrO_2 compounds (CZ55-1, CZ55-2 and CZ55-3), all having the same composition (Ce/Zr = 1): CZ55-1 was prepared by precipitation with aqueous NH_3 using CeO_2 powder (Anan Kasei Co., Ltd., 99.9%, 120 m^2/g) and aqueous $ZrO(NO_3)_2$ solution. The precipitate was dried at 90 °C and calcined in air at 500 °C for 3 h. CZ55-2 was prepared by coprecipitation with aqueous NH_3 using aqueous $Ce(NO_3)_3$ and $ZrO(NO_3)_2$ solutions. The precipitate was dried at 90 °C and calcined in air at 500 °C for 3 h. CZ55-3 was synthesized by the same coprecipitation process as CZ55-2, except that the dried powder was reduced at 1200 °C for 4 h in flowing pure CO and oxidized in air at 500 °C for 3 h. By using the conventional wet impregnation with $Pt(NH_3)_2(NO_2)_2$ aqueous solution, 1 wt% Pt/CeO_2–ZrO_2 compounds (CZ55-1, CZ55-2 and CZ55-3) catalysts were prepared. The impregnated powders were dried overnight at 110 °C and calcined at 500 °C for 3 h in air.

2.1.2. Characterization

The OSC was estimated by thermo-gravimetric (TG) analysis [14]. The 1 wt% Pt/CeO_2–ZrO_2 samples were cyclically reduced by 20% H_2/N_2 for 5 min, and then oxidized by 50% O_2/N_2 for 5 min at 500 °C. The weight loss and gain were measured using a thermo-gravimetric analyzer (TGA-50, Shimadzu Corp.). The reductive/oxidative conditions were maintained until the weight became constant. The value of the weight change between the reductive and oxidative conditions corresponds to the saturated OSC at 500 °C.

The specific surface areas of the samples were estimated using the N_2 adsorption isotherm at −196 °C by the one-point Brunauer–Emmett–Teller (BET) method using an automatic surface analyzer (Micro Sorp 4232II, Micro Data Co., Ltd.). The samples were degassed in flowing N_2 at 200 °C for 20 min.

Powder XRD experiments were carried out using a RINT2000 (Rigaku Co., Ltd.) diffractometer with Cu Kα radiation (1.5406 Å).

In situ time-resolved energy-dispersive XAFS was employed to investigate the redox behaviour of the CZ55 samples. The DXAFS spectra at Ce K-edge (40.45 keV) were measured in transmission mode at BL28B2 of SPring-8 (Hyogo, Japan). The main equipment in this study consists of a polychromator set to a Laue configuration with net plane Si(4 2 2) and a position-sensitive detector (PSD) mounted on a θ–2θ diffractometer. The sample of 90 mg was pressed into a pellet with 10 mm in diameter and then placed in an in situ quartz cell. As for the oxygen release process in Pt/CeO_2–ZrO_2 samples, after an oxidizing pre-treatment with 20% O_2/He at 500 °C for 30 min, the sample was heated from 50 to 500 °C with 5 °C/min in flowing 5% H_2/He (100 cc/min) at atmospheric pressure. Ce K-edge XAFS spectra measured for 0.4 s were accumulated 50 times in every 10 °C. The oxygen storage process was also investigated in the same way. After a reducing pre-treatment with 5% H_2/He at 500 °C for 30 min, the sample was heated from 50 to 500 °C with 5 °C/min in flowing 5% O_2/He (100 cc/min). Reagent grade CeO_2 was used for a standard Ce^{4+} spectrum, and Ce(III)AlO_3 for a Ce^{3+} spectrum.

2.2. Study of Pt sintering inhibition and Pt reduction

2.2.1. Preparation

Pt/Al_2O_3, Pt/MgO and Pt/ceria-based mixed oxide (Ce–Zr–Y mixed oxide, referred to as CZY) catalysts were prepared by the following methods. MgO (Ube Material Industries) and γ-Al_2O_3 (Nikki Universal Co., Ltd.) were used as support oxides. CZY powders was prepared using a coprecipitation process with aqueous NH_3 using $Ce(NO_3)_3$, $ZrO(NO_3)_2$ and $Y(NO_3)_3$ in aqueous solutions. The precipitate was dried at 110 °C and calcined in air at 700 °C for 3 h. CZY contains 50 wt% CeO_2, 46 wt% ZrO_2 and 4 wt% Y_2O_3, and its crystal structure was cubic. 1 or 2 wt% Pt supported catalysts were prepared by the conventional wet impregnation of Al_2O_3, MgO and CZY powders with $Pt(NH_3)_2(NO_2)_2$ aqueous solution (Tanaka Kikinzoku Kogyo K.K.). The impregnated powders

were dried overnight at 110 °C and calcined at 500 °C for 3 h in air. These samples are referred to as "fresh catalyst". Portion of the fresh sample were aged in air for 5 h at 800 °C. This ageing treatment corresponds to an accelerated test for durability in an oxidative atmosphere. These samples are referred to as "aged catalyst".

2.2.2. Characterization

The average particle size of Pt metal was measured using a CO pulse adsorption method [15]. The catalysts were pre-treated in flowing pure oxygen, and then pure hydrogen at 400 °C. With this reductive treatment of hydrogen, Pt is reduced to Pt metal. CO pulse adsorption was carried out in flowing He at −78 °C. At this temperature, the CO uptake on ceria support was almost entirely suppressed, and CO was adsorbed to only the surface of Pt [16]. The average particle size was calculated from CO uptake assuming that CO was adsorbed on the surface of spherical Pt particles at CO/(surface Pt atom) = 1/1 stoichiometry.

The powder XRD experiments were carried out in air at room temperature using a RINT2000 (Rigaku Co. Ltd.) diffractometer with Cu Kα radiation (1.5406 Å). The average particle size of Pt was estimated from the Pt(1 1 1) line width using Scherrer's equation with the Gaussian line shape approximation.

Three types of XAFS techniques were applied to the study of Pt supported catalyst. First, a conventional step-scan XAFS was used to determine the precise local structure around Pt in the Pt supported catalysts. The Pt L_3-edge (11.5 keV) XAFS measurement was carried out at BL01B1 and BL16B2 of SPring-8 (Hyogo, Japan). The XAFS spectra at Pt L_3-edge were measured using a Si(1 1 1) double crystal monochromator in the fluorescence mode at room temperature in air. Data reduction of the XAFS was carried out as described elsewhere [17]. Fourier transforms (FTs) were performed on the Pt L_3-edge EXAFS spectra in about 3.0–16 $Å^{-1}$ region. The inversely Fourier filtered data for the Pt–oxygen and Pt–cation (cation = Pt, Ce, Zr and Mg) peaks were analyzed with a curve-fitting method in the k range of 4–12 $Å^{-1}$ region for the Pt–oxygen, and 4–14 $Å^{-1}$ region for the Pt–cation, respectively. The theoretical parameters calculated by McKale et al. [18] were applied to the curve-fitting analysis. Absorption edge energy was fixed to a certain value, and then the coordination number (CN), the bond distance (R) and Debye–Waller factor (σ) were varied as adjustable parameters to obtain the best fit to the experimental data. Next, in situ time-resolved DXAFS for Pt/MgO and Pt/Al_2O_3 samples and Turbo-XAS (T-XAS) for Pt/CZY sample were used to investigate the reduction speed of Pt in the Pt supported catalysts. The DXAFS measurement was made at NW2A of PF-AR. The Pt L_3-edge XANES spectra were measured in transmission mode every 0.2 s using a Si(3 1 1) polychromator with a Bragg configuration and a 1024 channel line photodiode. On the other hand, the Pt L_3-edge XANES spectra for Pt/CZY catalyst were measured at the ID-24 of ESRF using the fluorescence yield variant of T-XAS developed by Pascarelli et al. at ID24 at the ESRF [19,20]. The Pt L_3-edge XANES spectra were collected every 2.0 s. At present, the combination of low levels of Pt in the catalysts, with high levels of heavy, absorbing, elements such as Ce and Zr severely compromises the conventional, transmission-based, DXAFS experiment. In order to obtain a window into the structural-reactive behaviour of the Pt in these systems with a sub second time resolution the fluorescence variant needs to be adopted as it permits Pt L_3-edge XANES on the required timescale even for these taxing samples. In both the DXAFS at PF-AR and the T-XAS at ESRF cases, specially designed in situ cells with rapid gas switching system were provided for the experiments. The dead volume of the cell was minimized, and the gases could be switched very quickly. Experimental procedures for the DXAFS at PF-AR and the T-XAS at ESRF were almost same as follows. The sample (40–60 mg) was pressed to a disk (5–7 mmϕ) and placed in an in situ cell. After an oxidizing pre-treatment with 20% O_2/He at 500 °C for 10 min, the gas was changed from 3% O_2/He (150 cc/min) into 3% H_2/He (150 cc/min) at a given temperature. Pt L_3-edge XANES spectra were recorded every about 0.2–2.0 s. PtO_2 powder was used for a standard Pt^{4+} spectrum, and Pt foil for a Pt^0 (metal) spectrum.

As for the Pt/CZY catalyst, the reduction behaviour of CZY support was also investigated. The DXAFS spectra at Ce K-edge were measured in transmission mode at BL28B2 of SPring-8. The XAFS measurement was made by same procedure as the previous section (see Section 2.1.2.).

3. Results and discussion

3.1. Study of redox behaviour of ceria–zirconia mixed oxides

3.1.1. Oxygen storage/release capacity, BET surface area and structural property

In our previous report, the physicochemical properties on CZ55-1, CZ55-2 and CZ55-3 were studied in detail [21]. The results are summarized in Table 1 and Fig. 1. The saturated OSC of 1 wt% Pt loaded Ce compounds was measured at 500 °C. The Pt accelerates the OSC speed especially during the oxygen release process, but the saturated OSC of the samples with and without Pt have the same value [14]. The OSC value increased in the order of CZ55-1 < CZ55-2 < CZ55-3. CZ55-3 exhibited the highest OSC. The BET surface areas ranged from 1 to 125 m^2/g. The BET surface areas depend on the preparation methods. Especially, the BET surface area of CZ55-3 is very low due to its high-temperature treatment during its synthesis, indicating that the OSC is not related to the surface area.

Based on XRD and XAFS analysis, model illustration of cation–cation network for the CeO_2–ZrO_2 samples is suggested in Fig. 1. CZ55-1 consists of pure CeO_2 and ZrO_2. A CeO_2–ZrO_2 solid solution forms in CZ55-2, but the Ce rich domain and Zr rich one still remain. The CeO_2–ZrO_2 solid solution in CZ55-3 homogeneously forms at an atomic level, and the crystal structure is cubic fluorite type which possesses the ordered arrangement of Ce and Zr ions along with <1 1 0> direction. The crystal structure of CZ55-3 is usually termed as "κ-$Ce_2Zr_2O_8$ phase" [22,23]. The κ-$Ce_2Zr_2O_8$ phase is prepared by mild-oxidation of the pyrochlore-type $Ce_2Zr_2O_7$, which maintains the ordered arrangement [22]. The OSC at 500 °C increases by enhancing the homogeneity of the Ce

Table 1
OSC property, BET surface area and phase identification by XRD.

Sample[a]	OSC[b] (μmol-O/g)	BET surface area (m^2/g)	Structure	Lattice parameter (Å)
CZ55-1	160	125	Cubic + tetragonal	5.41 (CeO_2) 3.58, 5.21 (ZrO_2)
CZ55-2	880	89	Cubic	5.29
CZ55-3	1500	1	Cubic κ-$Ce_2Zr_2O_8$[c]	5.26

[a] For sample description, see Section 2.
[b] Saturated oxygen storage/release capacity (OSC) value measured at 500 °C.
[c] Cubic fluorite structure which possesses the ordered arrangement of Ce and Zr ions along with <1 1 0> direction.

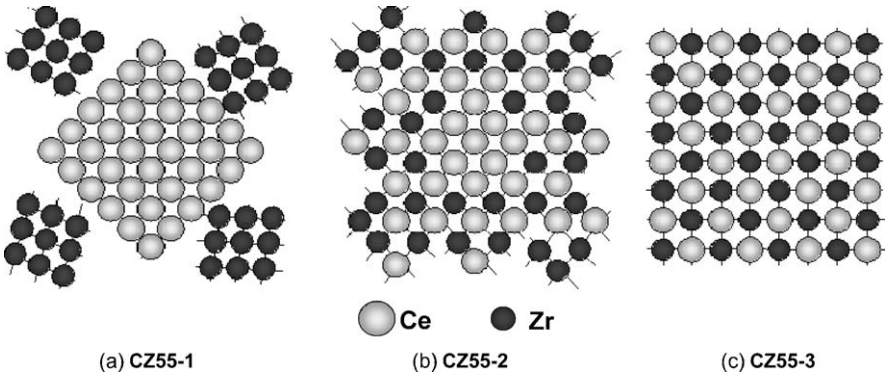

Fig. 1. Model illustration of cation–cation network for the CeO_2–ZrO_2 samples proposed by XAFS and XRD study.

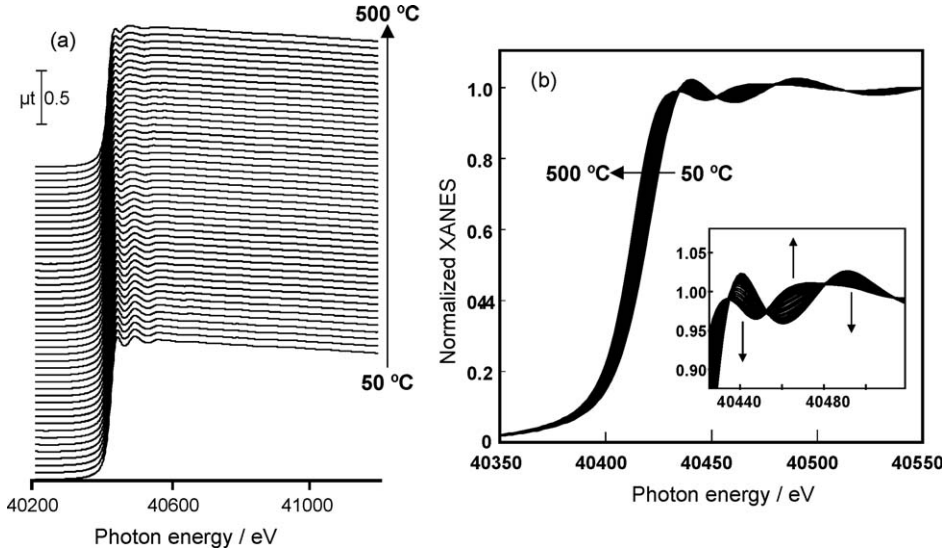

Fig. 2. Serial energy-dispersive (a) raw XAFS spectra and (b) normalized XANES at Ce K-edge during the oxygen release of Pt/CZ55-3 as a function of temperature in flowing 5% H_2/He. Measurements were made at BL28B2 of SPring-8.

and Zr atoms in the CeO_2–ZrO_2 solid solution. Especially, an atomically homogeneous κ-$Ce_2Zr_2O_8$ solid solution exhibited the highest OSC among these CeO_2–ZrO_2 samples.

3.1.2. Oxygen release behaviour

Fig. 2 shows an example of serial time-resolved Ce K-edge XAFS spectra of Pt/CZ55-3 in an oxygen release process at various temperatures in flowing 5% H_2/He. The spectra with a good signal-to-noise ratio at Ce K-edges could be obtained in the wide region up to EXAFS range. The XAFS measurement of the Ce K-edge with a wide electron wavenumber (k) range is required to obtain precise information on the Ce–Ce and Ce–Zr bonding, and to clarify the cation–cation network, because the usable data region of Ce L_3-edge EXAFS is limited to ca. 3–9 $Å^{-1}$ in k due to the presence of the Ce L_2-edge [21]. At present, we need a further investigation into the local structure around Ce and Zr in these samples, therefore, in this report, we will focus on the Ce K-edge XANES to study the valence change of Ce during oxygen release/storage processes. In Fig. 2(b), the spectra clearly demonstrate a change in the Ce oxidation state as a function of temperature. The serial XANES spectra exhibited isosbestic points, and the absorption edge energy shifted to lower energy. This indicates that the oxidation state of the Ce changes directly from Ce^{4+} to Ce^{3+} state. Absorption edge energy as a function of reduction temperature for Pt/CZ55-1, Pt/CZ55-2 and Pt/CZ55-3 are shown in Fig. 3. The percent of Ce reduction was evaluated using the following equation:

$$C_{Ce^{3+}}(\%) = \frac{E_{Ce^{4+}} - E_{obs}}{E_{Ce^{4+}} - E_{Ce^{3+}}} \times 100 \quad (1)$$

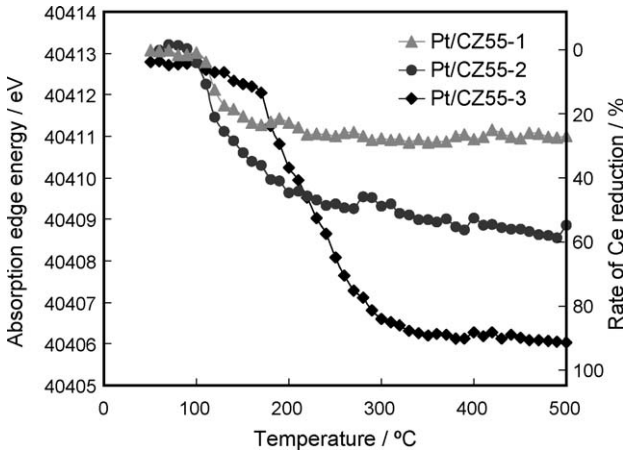

Fig. 3. Energy shift of Ce K-edge and corresponding percent Ce reduction for different samples during the oxygen release as a function of temperature in flowing 5% H_2/He.

where $C_{Ce^{3+}}$, $E_{Ce^{4+}}$, E_{obs} and $E_{Ce^{3+}}$ represent percent of Ce reduction, absorption edge energy of CeO_2 as a Ce^{4+} standard, observed absorption edge energy and absorption edge energy of $CeAlO_3$ as a Ce^{3+} standard. In addition, it is confirmed by XAFS and XRD analysis that the structural properties of these CZ samples are stable within the measurement temperatures of 50–500 °C in this study. The initial oxidation state of Ce at 50 °C was Ce^{4+} for every sample. The reduction of Ce^{4+} to Ce^{3+} in Pt/CZ55-1 begun to occur at around 100 °C, and then the percent Ce reduction got to 27%, and the value of the Ce reduction was constant at 200 °C and above. The Ce reduction in Pt/CZ55-2 also started at around 100 °C and the Ce reduction gradually increased at 200 °C or greater. The percent Ce reduction for the Pt/CZ55-2 came to about 60% at 500 °C. As for the Pt/CZ55-3, the Ce reduction arose at 100 °C, but its rate was a little bit compared to the Pt/CZ55-1 and Pt/CZ55-2. There was an immediate sharp increase of the Ce reduction at 170 °C or greater, and the percent Ce reduction in Pt/CZ55-3 came to about 90% at 300 °C.

The number of surface Ce atoms can be estimated to be ca. 6 μmol-Ce/m^2 for CeO_2–ZrO_2 (Ce:Zr = 1:1 molar ratio) [24]. The experimental values of BET surface area per gram of the samples were 125, 89 and 1 m^2/g for CZ55-1, CZ55-2 and CZ55-3, respectively. The amounts of Ce exposed to the surface are 750, 534 and 6 μmol-Ce/g, respectively. Therefore, it is estimated that the ratios of surface Ce to all Ce atoms are ca. 22.1, 15.8 and 0.2% for CZ55-1, CZ55-2 and CZ55-3, respectively. In the case of the Pt/CZ55-1, the percent Ce reduction at 500 °C in Fig. 3 (27%) is closed to that of the percent of surface Ce atoms (22.1%). This indicates that the Ce reduction of Ce^{4+} to Ce^{3+} in the Pt/CZ55-1 is limited only to the surface. On the contrary, the Ce reduction for Pt/CZ55-2 progresses from the surface to ca. 3 or 4 layers. For Pt/CZ55-3, almost all the bulk Ce atoms can be reduced from Ce^{4+} to Ce^{3+} state, because the percent of surface Ce for CZ55-3 is little or nothing. The Ce reduction for Pt/CZ55-1 and Pt/CZ55-2 with a high surface area commenced at 100 °C. On the other hand, that for Pt/CZ55-3 which possesses almost no surface area increased rapidly at 170 °C. It follows from these results that the reduction of surface Ce would mainly occur in the range 100–170 °C, and that the reduction of bulk Ce would progress at high temperatures of 170 °C and above. Fernández-García et al. clearly demonstrated the effect of particle size on OSC behaviour [35], it is reported that CeO_2–ZrO_2 nanoparticles interact with H_2 and reduce at lower temperatures than sintered CeO_2–ZrO_2 systems. The particle size of CeO_2–ZrO_2 sample corresponds to the surface area in this study. From the above results, it is suggested that the Ce reduction behaviour depends not only on the homogeneity of the Ce and Zr for bulk reduction at high temperatures but also on the particle size of the CeO_2–ZrO_2 samples for surface reduction at low temperatures.

Next, the relationship between the OSC and the Ce reduction in these samples was investigated. Fig. 4 presents the relationship between the OSC at 500 °C estimated by TG analysis in Table 1 and the percent Ce reduction at 500 °C calculated from the absorption edge energy at Ce K-edge in Fig. 3. The broken line in Fig. 4 is the theoretical value of OSC calculated from the percent Ce reduction according to the redox reaction ($CeO_2 \leftrightarrow CeO_{2-x} + x/2O_2$; x = 0–0.5). As a whole, there is the good linear relationship between OCS and percent Ce reduction though the OSC value of Pt/CZ55-1 is a little lower than that of the theoretical value. At present, the cause of the lower OSC value than the theoretical value in Pt/CZ55-1 is unclear. It is reasonable that only the Ce^{3+}/Ce^{4+} redox couple contribute to the OSC. In fact, The Zr oxidation state in CeO_2–ZrO_2 mixed oxides remains at Zr^{4+} under both the reductive and oxidative conditions at 500 °C [25,34].

3.1.3. Oxygen storage behaviour

The oxygen storage process through the Ce oxidation ($Ce^{3+} \rightarrow Ce^{4+}$) was studied in Pt/CZ55-3. There was no clear change of the Ce oxidation for Pt/CZ55-1 and Pt/CZ55-2 samples, the Ce oxidation state of Ce after a reducing pre-treatment had become already Ce^{4+} at 50 °C in flowing 5% O_2/He. Since the Pt/CZ55-1 and Pt/CZ55-2 have high surface areas, active surface Ce^{3+} species might have reacted with oxygen in the gas phase during the standby state at 50 °C before the temperature rising period. Fig. 5 shows absorption edge energy and corresponding percent Ce oxidation as a function of oxidation temperature for Pt/CZ55-3. The percent of Ce oxidation was evaluated using the following equation:

$$C_{Ce^{4+}}(\%) = \frac{E_{obs} - E_{Ce^{3+}}}{E_{Ce^{4+}} - E_{Ce^{3+}}} \times 100 \quad (2)$$

where $C_{Ce^{4+}}$ represents percent of Ce oxidation, and other terms are the same as those in Eq. (1). In Fig. 5, the Ce oxidation does not increase monotonously, but the Ce oxidation curve can be divided into two regions. One is the immediate sharp increase at 200 °C and below, and the other is the slight increase at 200 °C and above. The percent Ce oxidation at 200 °C is about 50%, and this value corresponds to the molecular formula of $Ce_2Zr_2O_{7.5}$. Sasaki et al. reported the existence of the metastable intermediate phase referred to as "β-$Ce_2Zr_2O_{7.5}$" using XRD, electron diffraction and thermo-gravimetric analysis [26]. The thermo-gravimetric curve reported by Sasaki was very similar to the Ce oxidation curve

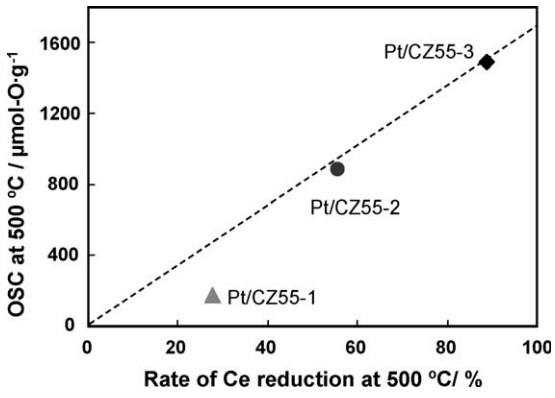

Fig. 4. Relationship between OSC estimated at 500 °C by thermo-gravimetric analysis and percent Ce reduction at 500 °C measured by Ce K-edge XANES. The broken line is the theoretical value of OSC calculated from the percent Ce reduction according to the redox reaction ($CeO_2 \leftrightarrow CeO_{2-x} + x/2O_2$; x = 0–0.5).

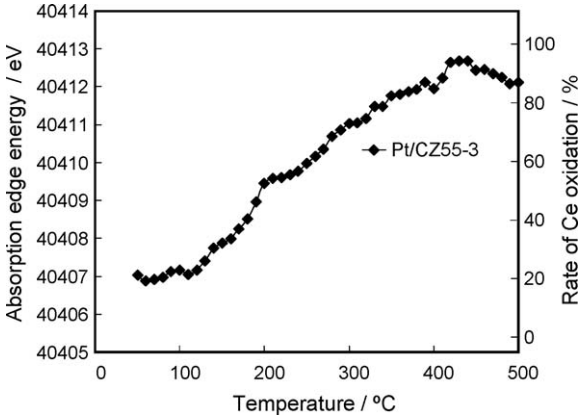

Fig. 5. Energy shift of Ce K-edge and corresponding percent Ce oxidation for Pt/CZ55-3 sample during the oxygen storage as a function of temperature in flowing 5% O_2/He.

Table 2
Average platinum particle size of the catalysts estimated by XRD and CO pulse adsorption method.

Sample[a]		Average Pt particle size (nm)	
		XRD[b]	CO pulse
Pt/Al_2O_3	Aged	61	23.6
Pt/MgO	Aged	ND[c]	9.6
Pt/CZY	Aged	ND[c]	1.1

[a] The amount of loaded Pt is 2 wt%.
[b] Average particle size was estimated from Pt(1 1 1) line width.
[c] The diffraction peak from the Pt particles could not be detected.

shown in Fig. 5. Our results by in situ XAFS analysis could support the evidence for the formation of β-$Ce_2Zr_2O_{7.5}$ intermediate phase from the view point of the change of Ce oxidation state. From these results, it was clear that the Ce oxidation speed from pyrochlore–$Ce_2Zr_2O_7$ to β-$Ce_2Zr_2O_{7.5}$ was faster than that from β-$Ce_2Zr_2O_{7.5}$ to κ-$Ce_2Z_2rO_8$.

3.2. Pt sintering inhibition and Pt reduction

3.2.1. Pt sintering inhibition

In our previous report, the sintering inhibition mechanism of Pt after high-temperature ageing in an oxidative atmosphere was studied [13,27]. In this report, we will investigate the comparison of sintering behaviour in Pt/Al_2O_3, Pt/MgO and Pt/CZY catalysts. The average size of Pt metal particles for the supported Pt catalysts after 800 °C ageing in air is summarized in Table 2. Pt particles in the Pt/Al_2O_3 grew up to large particles during the ageing treatment. The Pt particle size in the aged Pt/Al_2O_3 determined by the XRD and CO pulse method was 61 and 23.6 nm, respectively. On the other hand, Pt particles in the Pt/MgO and Pt/CZY could not be observed by XRD even after the ageing, suggesting that the Pt particles on MgO and CZY supports were highly dispersed. The Pt particle size in the aged Pt/CZY estimated by CO pulse was 1.1 nm. Though the Pt particles on MgO could not be observed by XRD, the average Pt particle size in the aged Pt/MgO estimated by CO pulse method was 9.6 nm. The contrariety in the Pt/MgO case is mainly to be attributed to high-stabilization of Pt oxide on MgO support. And more specifically, the Pt particles on the MgO support was not fully reduced to Pt metal particles during the pre-treatment of CO pulse method. The result in the following section would support the incomplete reduction of Pt particles on the MgO. Therefore, it was possible that the precise particle size could not estimate using CO pulse analysis. In any case, it is obvious that Pt particles on MgO and CZY support hardly sinter at all after the oxidative ageing treatment.

Fourier transforms of the supported Pt catalysts after 800 °C ageing in air and reference samples are presented in Fig. 6. The

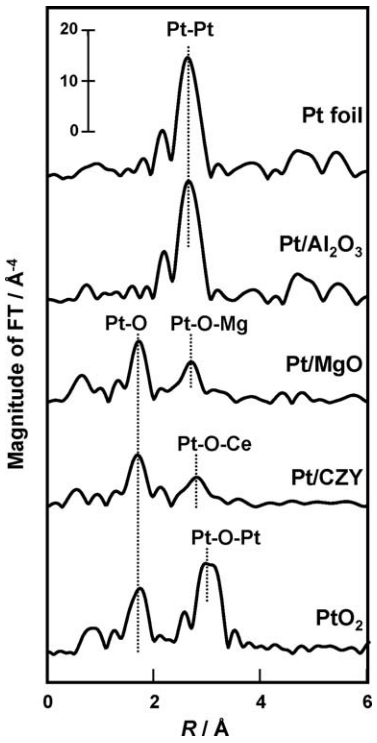

Fig. 6. Fourier-transformed k^3x data of Pt L_3-edge EXAFS for supported 2 wt% Pt catalysts after 800 °C ageing in air and the standard samples of Pt foil and PtO_2 powder. The XAFS measurement was curried out at room temperature in air, at BL01B1 and BL16B2 of SPring-8.

results of curve-fitting analysis are summarized in Table 3. The FT of the Pt/Al_2O_3 after the ageing was obviously different from those of the Pt/MgO and Pt/CZY. As for the aged Pt/Al_2O_3, only the intense peak at 2.76 Å, which corresponds to the Pt–Pt bond, was observed. The FT spectrum of the Pt/Al_2O_3 was coincided with that of Pt foil. The CN of the Pt–Pt shell in the aged Pt/Al_2O_3 was 11.5. This indicates that the Pt metal particles on Al_2O_3 after the ageing are at least 20 nm in size [31]. In the Pt/MgO and Pt/CZY after the ageing, these FT spectra were different from those of both Pt foil and PtO_2 powder. The position of the first peak at 2.02 Å in the Pt/MgO and Pt/CZY was close to that of PtO_2, and this peak was fitted with the Pt–O bond. It should be noted that the second evident peaks for the Pt/MgO and Pt/CZY were fitted with the Pt–Mg and Pt–Ce,

Table 3
Results of curve-fitting analysis for the aged catalysts and standard samples.

Sample[a]		Shell	CN	R (Å)	σ^2 (Å^2)
Pt foil[b]		Pt–Pt	12.0	2.76	0.0045
Pt/Al_2O_3	Aged	Pt–Pt	11.5	2.76	0.0046
Pt/MgO	Aged	Pt–O	5.9	2.04	0.0041
		Pt–Mg	6.2	3.02	0.0027
Pt/CZY	Aged	Pt–O	4.1	2.02	0.0007
		Pt–Ce	3.5	3.01	0.0037
PtO_2[b]		Pt–O	5.7	2.04	0.0026
		Pt–Pt	5.3	3.10	0.0019

[a] The amount of Pt supported on various supports is 2 wt%.
[b] The curve-fitting analysis for the standard samples were performed by reference to [32,33].

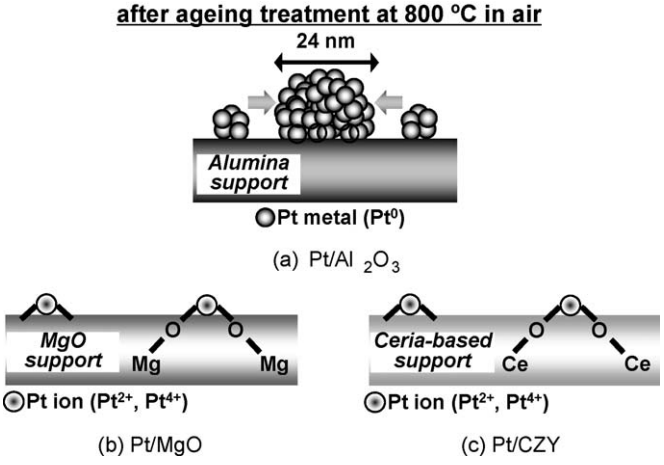

Fig. 7. Schematic illustration of the Pt supported catalysts after 800 °C ageing in air.

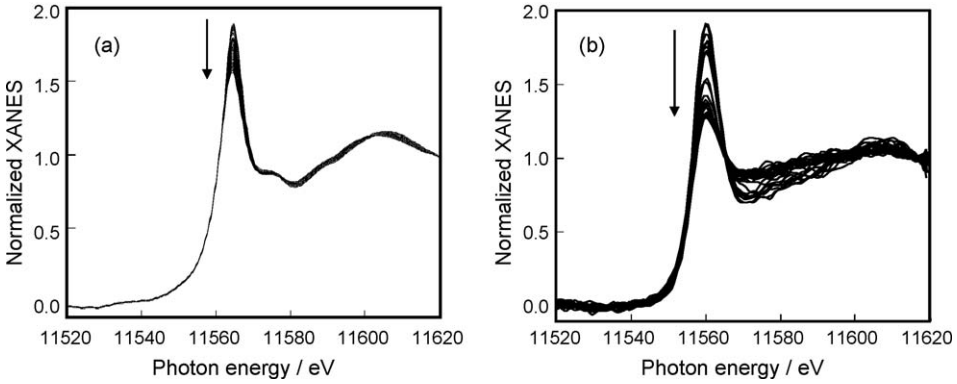

Fig. 8. Serial Pt L_3-edge XANES spectra through the switching of the gases from 3% O_2/He gas to 3% H_2/He gas. (a) Spectra for aged 1 wt% Pt/MgO catalyst measured by DXAFS in transmission mode at NW2A of PF-AR. Acquisition time is 0.2 – 1.0 s per spectrum. Measurement temperature is 400 °C. (b) Spectra for aged 1 wt% Pt/CZY catalyst measured by Turbo-XAFS in fluorescence mode at ID-24 of ESRF. Acquisition time is 2.1 s per spectrum. Measurement temperature is 150 °C.

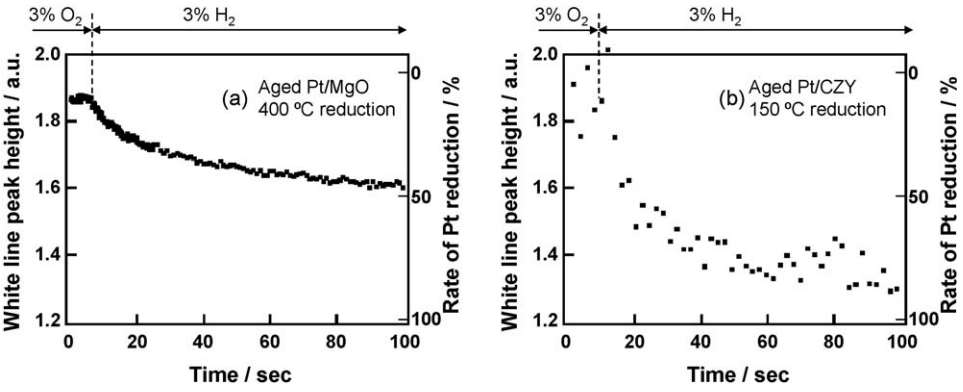

Fig. 9. Temporal dependences of the of the white line peak height of the Pt L_3-edge XANES and corresponding percent Pt reduction through the switching of the gases from 3% O_2/He gas to 3% H_2/He gas for (a) aged 1 wt% Pt/MgO and (b) aged 1 wt% Pt/CZY catalysts. Measurement temperatures for (a) and (b) are 400 and 150 °C, respectively.

respectively. These results lead to the conclusion that Pt atoms strongly interact with the MgO or CZY support during the ageing and form Pt–O–M (M = Mg, Ce) bond.

Based on our observation above, we proposed the sintering inhibition mechanism of Pt supported on MgO and CZY as shown in Fig. 7. In the case of Pt/Al_2O_3, since the interaction between Pt and Al_2O_3 is weak, Pt particles transport across the surface of the Al_2O_3 support and sinter during an 800 °C ageing treatment in an oxidizing atmosphere according to the molecular migration model [7,28,29]. In contrast, Pt supported on MgO or CZY has a strong interaction with their supports. Therefore these supports stabilize a high valence state (Pt^{2+} or Pt^{4+}) of Pt, and then the formation of the rigid Pt–O–M bond acts as an anchor. The formation of the Pt–O–M bond suppressed the sintering of Pt. It is considered that the highly dispersed Pt oxide on the surface of MgO or CZY support under oxidizing condition are more stable since the Pt–O–M bond energies are greater than the Pt–Pt bond energies in large Pt crystallites.

3.2.2. Pt reduction

In the previous section, it was clear that MgO and CZY supports could stabilize a high valence state of Pt after an oxidative ageing. However, it is considered that Pt^0 (metal) is the active site for the catalytic reaction in automotive exhaust condition. Therefore, Pt on the support has to be reducible during the catalytic reaction. Fig. 8 shows serial Pt L_3-edge XANES spectra through the switching of the gases from 3% O_2/He gas to 3% H_2/He gas. Fig. 8(a) and (b) are the spectra for aged Pt/MgO at 400 °C and aged Pt/CZY at 150 °C, respectively. The spectra clearly demonstrate a change in the Pt oxidation state as a function of time. White line peak height as a function of time for Pt/MgO and Pt/CZY are shown in Fig. 9. The percent of Pt reduction was estimated from the observed white line peak height on the basis of Pt foil and PtO_2 as correlation samples, in the same way as the study of Ce K-edge. In Fig. 9, though the reduction temperature in the aged Pt/CZY (150 °C) catalyst was

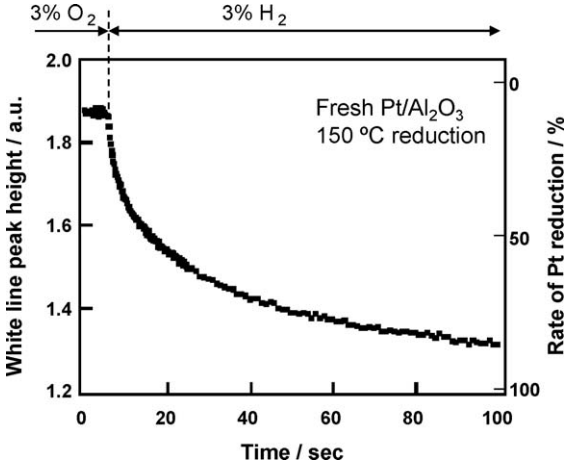

Fig. 10. Temporal dependences of the of the white line peak height of the Pt L_3-edge XANES and corresponding percent Pt reduction through the switching of the gases from 3% O_2/He gas to 3% H_2/He gas at 150 °C for fresh 1 wt% Pt/Al_2O_3 catalyst.

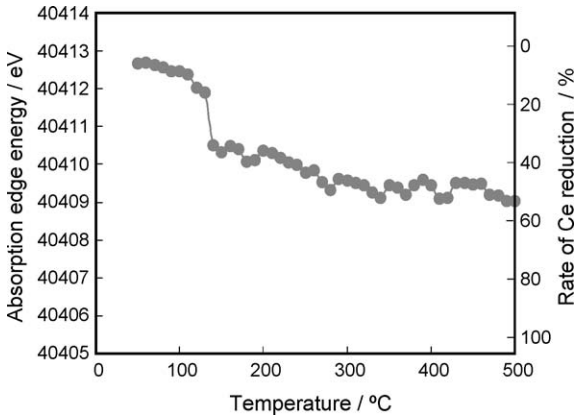

Fig. 11. Energy shift of Ce K-edge and corresponding percent Ce reduction for the fresh 1 wt% Pt/CZY catalyst during the oxygen release as a function of temperature in flowing 5% H_2/He.

low compared with the aged Pt/MgO (400 °C), the speed of Pt reduction for the Pt/CZY was significantly higher than that for the Pt/MgO. In addition, it is noteworthy that the Pt reduction speed for the aged Pt/CZY is almost same as that for fresh Pt/Al_2O_3 catalyst with Pt particle size of ca. 1 nm (Fig. 10). It has been reported that basic supports such as MgO, La_2O_3 and ceria-based oxide stabilize a high valence state of Pt, compared with acidic supports such as SiO_2, Al_2O_3 [13,30]. One explanation for the easiness of Pt reduction in Pt/CZY may be that other property of the CZY support, except for the basicity, work on the Pt reduction.

3.2.3. Reduction behaviour of CZY support

In order to clarify the cause of the easiness of Pt reduction in Pt/CZY, we investigate the reduction behaviour of CZY support that possesses the OSC function. Fig. 11 presents absorption edge energy at Ce K-edge as a function of reduction temperature for fresh Pt/CZY catalyst. Experimental procedure and analysis were performed in the same way as the previous section of CeO_2–ZrO_2 study. The Ce reduction in Pt/CZY started at around 100 °C and the Ce reduction gradually increased at 200 °C or greater. Finally, the percent Ce reduction for the Pt/CZY came to about 60% at 500 °C. The molar ratio of Ce to (Zr + Y) in the CZY support is 0.74, and its BET surface area was 99 m^2/g. The ratio of surface Ce atoms in the CZY, which was estimated roughly by same way as the CZ55 samples, is about 13%. It is considered that the surface Ce atoms in the CZY support are fully reduced from Ce^{4+} to Ce^{3+} at 150 °C since the percent Ce reduction of the CZY at 150 °C surpassed 20%.

3.2.4. Compatibility between the inhibition of Pt sintering and ease of Pt reduction in Pt/CZY

Based on our observation above, we proposed the compatibility between the inhibition of Pt sintering and the ease of Pt reduction in Pt/CZY as shown in Fig. 12. During an 800 °C ageing treatment in an oxidizing atmosphere, the Pt–O–M anchor on both MgO and CZY supports suppressed the sintering of Pt. On the other hand, during a usual operation such as stoichiometric and reducing conditions, the Pt–O–Ce^{4+} bond on the CZY support breaks easily through the reduction of Ce ($Ce^{4+} \rightarrow Ce^{3+}$) and then new small particles of Pt metal with high catalytic activity are formed. On the contrary, the Pt particles on the MgO support is not fully reduced to Pt metal particles even during the stoichiometric and reducing conditions. It is reasonable to suppose that the valence change of $Ce^{4+} \leftrightarrow Ce^{3+}$ cleverly controls the formation/release of Pt–O–Ce bond. This function would enable the compatibility between the inhibition of Pt sintering and the ease of Pt reduction in Pt/CZY.

4. Conclusion

In this study, we have utilized modern XAFS techniques for the dynamic in situ observation of automotive catalysts. First, we investigated the oxygen storage/release behaviours of CeO_2–ZrO_2 mixed oxides with different oxygen storage/release capacities and different structural properties. Secondly, we studied Pt sintering inhibition and Pt reduction in Pt supported catalysts. The results obtained are as follows:

(1) OSC of CeO_2–ZrO_2 mixed oxides
   (a) The Ce reduction behaviour depends not only on the homogeneity of the Ce and Zr for bulk reduction at high temperatures but also on the particle size of the CeO_2–ZrO_2 samples for surface reduction at low temperatures.
   (b) The reduction of surface Ce mainly occurred in the range 100–170 °C, and the reduction of bulk Ce progressed at high temperatures of 170 °C and above.
   (c) There was a good linear relationship between the OCS measured by thermo-gravimetric analysis and the percent Ce reduction estimated from the absorption edge energy at Ce K-edge, suggesting that the Ce^{3+}/Ce^{4+} redox couple contribute to the OSC.
   (d) The observation of the change of Ce oxidation state during the oxygen release process indicated the evidence for the existence of β-$Ce_2Zr_2O_{7.5}$ intermediate phase.

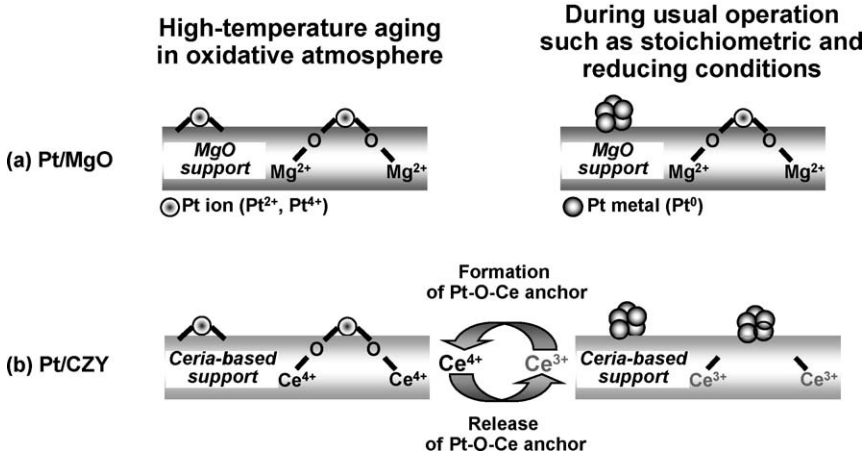

Fig. 12. Schematic illustration of the Pt anchor site for Pt/MgO and Pt/CZY catalysts.

(e) The Ce oxidation speed from pyrochlore–$Ce_2Zr_2O_7$ to β-$Ce_2Zr_2O_{7.5}$ was faster than that from β-$Ce_2Zr_2O_{7.5}$ to κ-$Ce_2Zr_2O_8$.

(2) Pt sintering inhibition and Pt reduction in Pt supported catalysts
   (a) We proposed that the Pt–O–M (M = Mg, Ce) bond acted as an anchor and inhibited the sintering of Pt particles on MgO or ceria-based oxide during 800 °C ageing in air.
   (b) The speed of Pt reduction for the aged Pt/CZY was significantly higher than that for the aged Pt/MgO.
   (c) The surface Ce atoms in the CZY support were fully reduced from Ce^{4+} to Ce^{3+} at 150 °C.
   (d) It was suggested that Pt–O–Ce^{4+} bond on the support breaks easily through the reduction of Ce ($Ce^{4+} \rightarrow Ce^{3+}$) during the usual stoichiometric and reducing conditions, that is, the valence change of Ce^{4+}/Ce^{3+} in the ceria-based oxide support cleverly controls the formation/release of Pt–O–Ce bond as appropriate.

Acknowledgements

The authors are grateful to Tomoya Uruga, Hajime Tanida, Shigeru Yokota (SPring-8), Sakura Pascarelli, Mark Newton, Bernard Gorges, Olivier Mathon, Sebastien Pasternak, Florian Perrin, Steven Fiddy (ESRF), Akane Suzuki, Yasuhiro Inada (KEK PF), Yasuo Ikeda, Naoyuki Hara, Muriel Lepage, Takashi Kuzuya (TOYOTA Motor Europe), Takeshi Hirabayashi, Nobuyuki Takagi, Masahide Miura (TOYOTA Motor corporation), Takamasa Nonaka, Akihiko Suda, Hideo Sobukawa, Toshitaka Tanabe, Naoki Takahashi, Satoshi Yamaguchi, Yoshiki Seno, Tsuyoshi Sasaki and Masahiro Sugiura (TOYOTA Central R&D) for their excellent work.

References

[1] S. Matsumoto, Catal. Today 90 (2004) 183.
[2] H.C. Yao, Y.F. Yao, J. Catal. 86 (1984) 254.
[3] M. Ozawa, M. Kimura, A. Isogai, J. Alloys Compd. 193 (1993) 73.
[4] S.H. Overbury, D.R. Huntley, D.R. Mullins, G.N. Glavee, Catal. Lett. 51 (1998) 133.
[5] T. Yamamoto, A. Suzuki, Y. Nagai, T. Tanabe, F. Dong, Y. Inada, M. Nomura, M. Tada, Y. Iwasawa, Angew. Chem. Int. Ed. 46 (2007) 9523.
[6] P.J.F. Harris, J. Catal. 97 (1986) 527.
[7] R.M.J. Fiedorow, B.S. Chahar, S.E. Wanke, J. Catal. 51 (1978) 193.
[8] C.H. Bartholomew, Appl. Catal. A 212 (2001) 17.
[9] H. Birgersson, L. Eriksson, M. Boutonnet, S.G. Järås, Appl. Catal. B 54 (2004) 193.
[10] E.C. Su, W.G. Rothschild, J. Catal. 99 (1984) 506.
[11] A.F. Diwell, R.R. Rajaram, H.A. Shaw, T.J. Truex, Stud. Surf. Sci. Catal. 71 (2001) 139.
[12] L.L. Murrell, S.J. Tauster, D.R. Anderson, Stud. Surf. Sci. Catal. 71 (2001) 275.
[13] Y. Nagai, T. Hirabayashi, K. Dohmae, N. Takagi, T. Minami, H. Shinjoh, S. Matsumoto, J. Catal. 242 (2006) 103.
[14] A. Suda, H. Sobukawa, T. Suzuki, T. Kandori, Y. Ukyo, M. Sugiura, J. Ceram. Soc. Jpn. 109 (2001) 177.
[15] T. Uchijima, Catalytic Science and Technology, Kodansha-VCH, Weinheim, 1990.
[16] A. Holmgren, B. Andersson, D. Duprez, Appl. Catal. B 22 (1999) 215.
[17] T. Tanaka, H. Yamashita, R. Tsutitani, T. Funabiki, S. Yoshida, J. Chem. Soc. Farad. Trans. 84 (1988) 2987.
[18] A.G. McKale, B.W. Veal, A.P. Paulikas, S.K. Chan, G.S. Knapp, J. Am. Chem. Soc. 110 (1988) 3763.
[19] S. Pascarelli, T. Neisius, S. De Panfilis, J. Synchrotron Rad. 6 (1999) 1044.
[20] Y. Nagai, N. Takagi, Y. Ikeda, K. Dohmae, T. Tanabe, G. Guilera, S. Pascarelli, M. Newton, H. Shinjoh, S. Matsumoto, AIP Conf. Proc. 882 (2007) 594.
[21] Y. Nagai, T. Yamamoto, T. Tanaka, S. Yoshida, T. Nonaka, T. Okamoto, A. Suda, M. Sugiura, Catal. Today 74 (2002) 225.
[22] T. Omata, H. Kishimoto, S. Otsuka-Yao-Matsuo, N. Ohtori, N. Umesaki, J. Solid. State Chem. 147 (1999) 573.
[23] H. Kishimoto, T. Omata, S. Otsuka-Yao-Matsuo, K. Ueda, H. Hosono, H. Kawazoe, J. Alloys Compd. 312 (2000) 94.
[24] T. Tanabe, A. Suda, C. Deccorme, D. Duprez, H. Shinjoh, M. Sugiura, Stud. Surf. Sci. Catal. 138 (2001) 135.
[25] P. Fornasiero, R. Di Monte, G. Rao Ranga, J. Kašpar, S. Meriani, A. Trovarelli, M. Granziani, J. Catal. 151 (1995) 168.
[26] T. Sasaki, Y. Ukyo, A. Suda, M. Sugiura, K. Kuroda, S. Arai, H. Saka, J. Ceram. Soc. Jpn. 111 (2003) 3820.
[27] T. Tanabe, Y. Nagai, K. Dohmae, H. Sobukawa, H. Shinjoh, J. Catal. 257 (2008) 117.
[28] R.M.J. Fiedorow, S.E. Wanke, J. Catal. 43 (1976) 34.
[29] P. Forzatti, L. Lietti, Catal. Today 52 (1999) 165.
[30] H. Yoshida, Y. Yazawa, N. Takagi, A. Satsuma, T. Tanaka, S. Yoshida, T. Hattori, J. Synchrotron Rad. 6 (1999) 471.
[31] R.B. Greegor, F.W. Lytle, J. Catal. 63 (1980) 476.
[32] M. Vaarkamp, Catal. Today 39 (1998) 271.
[33] A.F. Lee, K. Wilson, R.M. Lambert, C.P. Hubbard, R.G. Hurley, R.W. McCabe, H.S. Gandhi, J. Catal. 184 (1999) 491.
[34] J.A. Rodriguez, X. Wang, G. Liu, J.C. Hanson, J. Hrbek, C.H.F. Peden, A. Iglesias-Juez, M. Fernández-García, J. Mol. Catal. A 228 (2005) 11.
[35] J.A. Rodriguez, J.C. Hanson, J. Kim, G. Liu, A. Iglesias-Juez, M. Fernández-García, J. Phys. Chem. B 107 (2003) 3535.